Investigation of the Electrochemical Active Surface Area and Lithium Diffusion in Graphite Anodes by a Novel OsO$_4$ Staining Method

Lukas Pfaffmann[a], Claudia Birkenmaier[b,c], Marcus Müller[a], Werner Bauer[a], Tim Mitsch[d], Julian Feinauer[d,e], Yvonne Krämer[d], Frieder Scheiba[a*], Andreas Hintennach[b], Thomas Schleid[c], Volker Schmidt[e] and Helmut Ehrenberg[a]

[a] *Institute for Applied Materials, Karlsruhe Institute of Technology, Herrmann-v.-Helmholtz-Platz 1, 76344 Eggenstein-Leopoldshafen, Germany*
[b] *Daimler AG, HPC G012, Hanns-Klemm-Str. 45, 71034 Böblingen, Germany*
[c] *Institute of Inorganic Chemistry, Stuttgart University, Pfaffenwaldring 55, 70569 Stuttgart, Germany*
[d] *Deutsche ACCUmotive GmbH & Co. KG, Neue Straße 95, 73230 Kirchheim unter Teck, Germany*
[e] *Institute of Stochastics, Ulm University, Helmholtzstr. 18, 89069 Ulm, Germany*

*Corresponding author: Phone: +49 721 60828520; Fax: +49 721 60828521;
e-mail: frieder.scheiba@kit.edu

Abstract

Negative electrodes of lithium-ion batteries generally consist of graphite-based active materials. In order to realize batteries with a high current density and therefore accelerated charging processes, the intercalation of lithium and the diffusion processes of these carbonaceous materials must be understood. Therefore, in this paper, we visualized the electrochemical active surface area for three different anode materials using a novel OsO$_4$ staining method in combination with scanning electron microscopy techniques. The diffusion behavior of these three anode materials was investigated by potentiostatic intermittent titration technique measurements. From those we determined the diffusion coefficient with and without consideration of the electrochemical active surface area.

1   Introduction

Nowadays, several stationary or transportation applications are provided with lithium-ion batteries (LiBs) [1]. Especially in an automotive context, these batteries are promising candidates due to their high energy and power density [2]. Although research and development is undertaken worldwide to establish advanced LiBs with improved electrochemical performance, graphite still represents the best choice as an anode material in commercial LiBs [3–5].

Graphite has a theoretical capacity of 372 mAh/g. During charging, lithium ions are intercalated between the graphite sheets and de-intercalated while discharging. Thus, various solid solutions with consistencies from an unlithiated state up to a maximum lithiation of LiC_6 are formed [5–8].

The kinetics of lithium diffusing into these graphite basal planes are strongly dependent on the carbon crystal structure and differ among the various carbon materials. In order to investigate the corresponding diffusion coefficient D_{Li}, the potentiostatic and galvanostatic intermittent titration techniques (PITT and GITT, respectively) developed by Weppner and Huggins [9] can be applied as suitable electroanalytical methods. Today, a multiplicity of data, determined through GITT or PITT methods for the diffusion coefficients of lithium either into graphitic materials or non-graphitic carbonaceous anodes, are reported [10]. These diffusion kinetics are determined by the crystal structure of the carbon material and therefore differ among the anode materials [3]. Thus, D must be calculated for each material individually. In this paper, focus is placed on the PITT method.

From GITT and PITT measurements, the diffusion constant D or other related quantities such as the diffusion length l or characteristic time-constant τ can be calculated by using the Cottrell equation as described in [11,12] . Typically, τ is calculated using the following equation 1,

Eq. 1
$$\tau = \frac{l^2}{D} = \left[\frac{Q_t \Delta X}{\pi^{\frac{1}{2}} I \, t^{\frac{1}{2}}}\right]^2,$$

with Q_t = the maximum amount of charge, X = the intercalation level, I = the current and t = the time.

The challenge with this method is that the characteristic diffusion length l is often unknown. As a simplified approach, the relation $l = V/S$, with the volume V and the surface S, can be used. This can be true in the case considered by Aurbach and Levi [11,12] for a foil-like electrode structure. However, actual electrodes have complex morphologies, whereby such a relation must be modified. In this case, the equation for the diffusion coefficient must be stated as…

Eq. 2
$$D = \left[\frac{I \, t^{\frac{1}{2}}}{S_{\text{EASA}} \, \Delta Q} \pi^{\frac{1}{2}} \cdot V_{\text{mass}}\right]^2,$$

…whereby V_{mass} is the complete usable volume of graphite active material and the S_{EASA} the active surface of the electrode, also referred to as the electrochemically active surface area (EASA). Here, active denotes that only a fraction of the overall surface contributes to the intercalation and the interface reaction. V_{mass} is easily accessible as it is equal to the overall volume of the anode active material and can be calculated using the mass of the sample divided by its specific density or considering the bounding volume and the porosity. The more crucial part is the measurement of the active surface that contributes to the interfacial exchange current density. The complete specific surface of a particulate material can be easily derived by the Brunauer-Emmett-Teller (BET) method. A comparison between the BET-specific area and the irreversible charge loss caused by solid electrolyte interface (SEI) formation frequently results in a linear relationship [5]. However, the BET method only provides an upper limit for the EASA since, due to the anisotropic microstructure of the carbon materials, not the entire area of the particles that is accessible to physical adsorption of

gas molecules also contributes to the lithium exchange. The EASA concept only takes into account defects of the graphite sheets and regards them as "active sites". The higher the ratio of EASA (more precisely, of active sites) of the overall graphite anode, the more reactive the graphite electrode [13]. At these sites, electrolyte decomposition reactions also take place that are responsible for SEI formation.

The detection of the lithium-containing reduction products at the EASA is hardly possible when utilizing electron microscopy techniques due to the low scattering contrast and instability of these compounds in the electron beam. The contrast can be increased when the anode is previously stained with osmium tetroxide as described in [14].

In this paper, the diffusion coefficient and the EASA for three different carbonaceous materials is reported. In the first step, an amorphous carbon material and two artificial graphite materials, differing only in particle size, were characterized. The EASA of all anode materials with a state of charge (SOC) of 0 %, 5 %, and 10 % were visualized and determined via scanning electron microscopy (SEM) after osmium tetroxide staining. Then, based on the PITT measurement results obtained, the D_{Li} for the lithium diffusion in the graphite anode material was simulated.

2 Experimental

2.1 Characterization of carbon active materials

To prepare the carbon anodes, artificial graphite with flake geometry and a spherical amorphous carbon were applied, both of which were supplied by SGL Carbon GmbH (Meitingen, Germany). The artificial graphite was available with two different grain sizes, whereby the finer material was obtained from the coarser powder through an additional milling step. In the following, the carbon samples are labeled AC (amorphous carbon), CG (coarse graphite), and FG (fine graphite).

The grain size distribution and BET-specific surface area of the carbon materials are summarized in table 1.

Table 1: Physical properties of carbon-active material.

Sample	Particle size distribution			BET surface
	d10 (µm)	d50 (µm)	d90 (µm)	m^2/g
CG	9	18	44	6.3
FG	6	9	14	11.9
AC	7	10	16	4.6

2.2 Electrode preparation and cell assembly

From each carbon material, electrode sheets were prepared containing additional carbon black (C-NERGY™ SUPER C65 from IMERYS), sodium carboxymethyl cellulose (CMC), (WALOCEL™ CRT from DOW Chemicals), and styrene-butadiene-rubber (SBR), (TRD 2001 from JSR Micro). The homogenized aqueous slurries were cast onto Cu foil using a continuous laboratory coater equipped with doctor-blade technology and a convection dryer. Electrodes of 12 mm in diameter were punched from the sheets. The electrodes were stored in a vacuum oven for at least 24 hours at 80 °C to remove residual moisture before the cells

were built in an argon-filled glove box with an oxygen and water concentration below 1 ppm. T-shaped, three-electrode Swagelok® cells were used for electrochemical cycling. Pure metallic-lithium foils were applied as counter (10 mm Ø) and reference (3 mm Ø) electrodes to enable precise control of the working electrode potential. Each lithium foil was electrically isolated from the graphite electrode by one sheet of glass fiber separator (13 mm Ø, Whatman) to avoid short circuiting of the cell. A quantity of 0.200 ml of a mixture of 1M $LiPF_6$ in ethylenecarbonate:dimethylcarbonate (EC/DMC) (1:1) served as electrolyte (LP30, BASF).

2.3   Electrochemical cycling

Electrochemical cycling was carried out inside a climate chamber at 25 °C using a multichannel potentiostat (VMP-3, BioLogic). The cells were galvanostatically cycled between 3 V and 0.005 V versus Li^+/Li with a current of C/20. The first cycling, from 3 V down to 0.005 V, is required for cell formation and building the solid electrolyte interface. The second step, from 0.005 V up to 1.8 V and back to 0.005 V, is used to acquire information about the real capacity. From there, the cells were discharged to the final SOCs of 0 %, 5 %, and 10 %. with a current of C/20. In the case of 0 %, the cells were discharged to 1 V versus Li^+/Li and held at 1 V until the current was less than 0.005 mA to ensure that all lithium is fully de-intercalated from the graphite. In all other cases, calculation of the SOC was based on the second-step cycling discharge capacity.

The cells for PITT measurements were cycled at 25 °C. A potential step of 5 mV was set if the current was less than 5 µA or the time of the last step exceeded 6 hours. The cycling was carried out from 3 V (open circuit voltage) down to 0.005 V and up to 1.8 V.

2.4   Osmium tetroxide staining

Handling for the osmium tetroxide staining was carried out as described in [14]. The osmium tetroxide staining was performed in a self-constructed sealed staining system that allows a safe storage and handling of the highly toxic OsO_4. The samples were put into this system in an argon atmosphere. The exposure time was chosen between 12 hours and 18 hours. After the exposure, the samples were sealed off from the OsO_4 crystals and the chamber was flushed with argon for at least two hours before sample removing.

2.5   Electrode characterization

For SEM investigation of porosity as well as texture (particle orientation) of the pristine electrodes, cross-sections were processed by using a triple ion-beam cutter system (EM TIC-3X, Leica-Microsystems) with argon as the working gas. This technique was also applied for the electrodes that had been charged to a certain SOC and subsequently treated with OsO_4 to estimate the active surface area of the different carbon materials.

An in-lens detector, an energy-selective backscattered (EsB) detector and an angle-selective backscatter (AsB) detector were used in a scanning electron microscope (ZEISS MERLIN) for the surface characterization of the graphite electrodes. For detector details, see [15,16]. The acceleration voltage was set to 10 keV and 7 keV, whereas the grid voltage of the EsB detector was set to 1.5 keV and 0.9 keV. The probe current was set to 168 pA. The values of brightness and contrast of the detectors were chosen to be the same for every image. To assure maximum comparability, the detector settings were kept identical for all SEM micrographs. For the EDX measurements, a QUANTAX 400 system from BRUKER was used.

3 Results and discussion

3.1 Electrode morphology

Preparing cross-sections via an ion milling technique has proven to be an extremely valuable tool for providing insight into the microstructure of the highly porous and fragile electrodes without producing noticeable preparation artefacts. Figure 1 presents SEM micrographs of ion-milled cross-sections of 120 μm thick anode layers. Images of the first row are overviews of the separator-oriented section of the electrode. The second row provides a more detailed expression of the carbon particles within the electrode layer. Obvious differences in the electrode morphology can be detected especially between the flake-like graphites (Figures 1 a, b, d, and e) and the spherical amorphous carbon (Figure 1 c+f). Due to their pronounced anisotropy, the graphite materials CG and FG reveal a preferred orientation parallel to the coating direction which is also parallel to the calendaring direction. In accordance with the finer particle size of FG, the corresponding electrode layer exhibits visually smaller pore radii (Figures 1 b+e). Irrespective of the different particle size, the layer texture and pore shape of both graphites appear quite similar. The spherical particles of the amorphous carbon underwent no plastic deformation or texturing during calendaring, resulting in an open-pore structure with relatively large pore sizes (Figures 1 c+f). It can be expected that the electrolyte easily penetrates the complete anode layer down to the current collector.

As Figures 1 d+e illustrate, the graphite samples FG and CG exhibit a substantial amount of visible porosity within the graphite particles. From the cross-sections, one cannot conclude to which extent such pores are accessible to the electrolyte and may form an SEI layer. In contrast, AC particles show no, or only negligible, porosity. Hence, the calculated porosity should be virtually identical to the porosity available for the electrolyte and Li transportation. (For the total amount of porosity before and after calendaring, electrode density, and areal mass loading, see the supplementary part.)
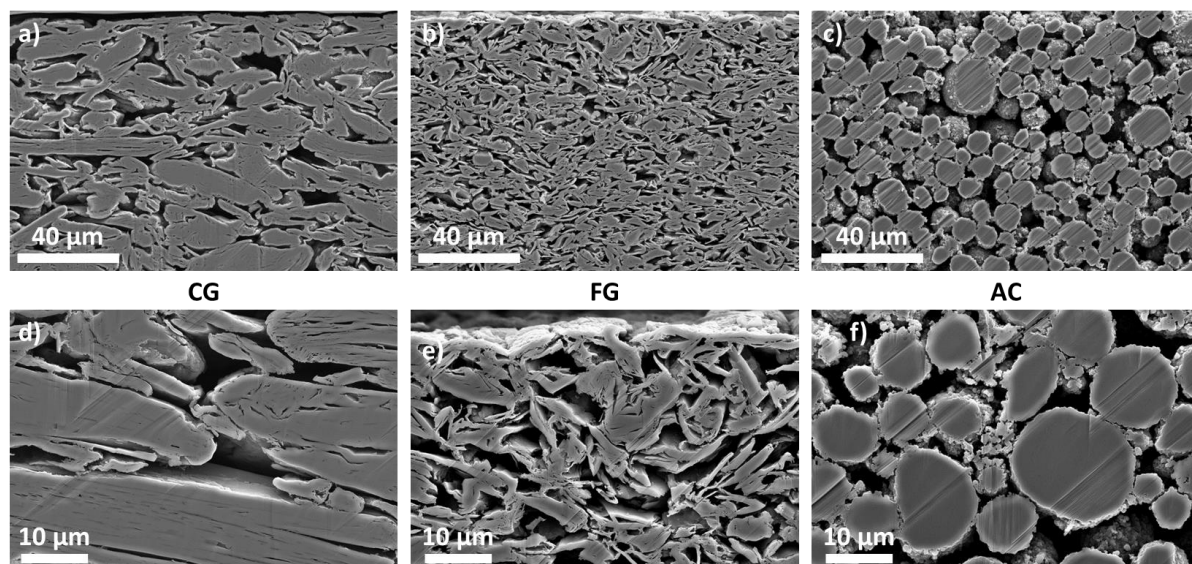
Figure 1: SEM micrographs of carbon anode cross-sections – prepared by ion milling; (a)+(d) CG, (b)+(e) FG, and (c)+(f) AC. Electrodes are calendared and vacuum dried before preparation.

3.2 SEM investigations of OsO_4 stained electrode

Osmium tetroxide is known to react with double bonds and as a strong Lewis acid may also attack carboxyl groups, alcohols, amines, esters and ethers. It has also been shown that osmium tetroxide reacts readily with metallic lithium and lithium intercalation compounds of graphite [14]. The reaction product appears to be a lithium osmate. However, its exact composition and structure could not be identified yet.

The reaction is so intense that the lithium will diffuse out of the graphite and the reaction products build islands on its surface. Since the reaction product is solid and lithium mobility on the graphite surface is low, it is expected that the islands form close to those parts of the surface where lithium can easily de-intercalate (intercalate) into the graphite particle. Hence, the distribution of the reaction products may serve as a visual marker of the electrochemical active surface area (EASA) of carbon electrodes for lithium-ion batteries.

3.2.1 Verification of Osmium in EsB and AsB images

The sensitivity of the different SEM detectors for the osmium reaction compounds is tested by recording SEM images of the same sample region of a stained graphite electrode with the InLens, EsB, AsB, and EDX detectors. The results are shown in Figure 2. The InLens detector (Figure 2a) clearly reveals the edges of particles but no osmium reaction compounds can be detected. Hence, the information gained by the InLens detector is purely topographic. In contrast, the EsB detector (Figure 2b) shows regions that appear brighter than others due to different energies of the backscattered electrons coming from these regions. Thus, the elemental composition is different. Similarly, the AsB detector (Figure 2 c) reveals regions of high backscattering contrast, but some areas that appear bright in the EsB image are darker or completely black. In general, the contrast is decreased. One reason for this is the fact that electrons originating from particles in a lower image plain cannot reach the AsB detector, because their scattering angle is too low. Another reason is that the brightness is thickness dependent, because the electron yield increases as the thickness increases. As a consequence, only the regions with a thicker layer of osmium reaction products appear bright. By comparing the SEM images in Figure 2 a) to c), the subsequent information can be gained by the actual detectors: InLens detector: topographic and surface contrast, also of lower-level particles. EsB detector: material contrast, also of lower-level particles as well as for thin composition layers. AsB detector: material contrast, but only of thick composition layers and no contrast of lower level regions.

To prove that the contrast in EsB and AsB images can be related to osmium-rich regions, EDX measurements are carried out for the same region. The resulting EDX maps of the element carbon, oxygen and osmium are shown in Figure 2 d) to f). The EDX measurement reveals higher concentrations of osmium and oxygen for the regions which appear bright in

the EsB and AsB images. Therefore, EsB and AsB imaging can be used to detect the osmium reaction compounds on the carbon electrodes.

3.2.2 OsO$_4$ stained graphite electrodes

To find the best conditions for OsO$_4$ staining, the different carbon electrode materials (FG, CG and AC) are charged to an SOC of 0 %, 5 % and 10 %. Also, uncycled graphite electrodes are stained with OsO$_4$ as a reference and to examine whether the SBR binder of the electrode reacts to a significant extent with the OsO$_4$ and therefore may lead to misinterpretation. InLens SEM images of the CG graphite electrode are shown in Figure 3 a) to d). The corresponding EsB image of the InLens image is below it. The contrast of the EsB image of the un-cycled stained electrode (Figure 3 e) is dramatically increased (100 %) at the SEM compared to the other EsB images (74 %), and it does not contain any bright areas that may be attributed to a reaction with OsO$_4$. Thus, the reaction between osmium tetroxide and the SBR binder has no significant influence on the electron contrast in EsB or AsB images. Compared to the uncycled electrode (Figure 3e), the particle edges parallel to the beam of the fully discharged electrode (SOC of 0 %, Figure 3 f) appear brighter. This effect can be attributed to the reaction of the OsO$_4$ vapor with parts of the solid electrolyte interphase (SEI) covering the graphite particles. Since the electron beam interacts with a larger SEI volume at the edges parallel to the beam their contrast is increased with respect to particle edges perpendicular to it. For the electrode charged to an SOC of 5 %, the contrast increases slightly (Figure 3 g) and some small bright islands appear. As expected, the sample with an SOC of 10 % shows the brightest contrast in the EsB image (Figure 3 h). Due to the staining, the edge sites of the particles where lithium can easily intercalate or de-intercalate are clearly highlighted. The OsO$_4$ staining technique may therefore be used to visually identify the electrochemically active surface area (EASA).

Cross-sections obtained by Ar-ion polishing are analyzed in order to verify whether the chosen time of 18 hours in the OsO_4 vapor is long enough to let all particles of the entire electrode react with the osmium tetroxide vapor (Figure 4). The AsB image (Figure 4 b) shows a uniform distribution of bright regions around the graphite particles, proving that the osmium tetroxide vapor readily penetrates into the entire electrode.

3.2.3 Electrochemical active surface area of different graphite electrodes

In the previous section, it could be demonstrated that the OsO_4 staining technique can be used to visually identify the EASA of carbon electrodes. Therefore, three different carbon electrodes (FG, CG and AC) are stained after charging to an SOC of 5 % and 10 % (Figure 5). As mentioned in section 2.5, the detector and image settings are kept identical for all samples. However, for FG with an SOC of 5 % (Figure 5 a), it is necessary to increase the brightness by 30 % afterwards due to the darkness of the raw image.

The results obtained for the two graphitic electrodes (Figure 5 a to d) are very similar except for the weaker contrasts of the 9 µm graphite sample as compared to the 20 µm sample. This effect can be easily explained by the larger surface area and, hence, greater edge site of the 9 µm sample, which requires more intercalated lithium to react with the OsO_4 vapor to yield the same electron contrast.

In contrast, the osmium is distributed much more homogeneously on the surface of the amorphous carbon. This corresponds well to the much more random orientation of graphite layers in the amorphous carbon. However, for the amorphous carbon as well, some parts of the surface show a lower quantity of osmium reaction products, indicating that even in the case of amorphous carbons, not the entire surface area is electrochemically active for lithium insertion/de-insertion.

For calculating the EASA cross-sections, samples are prepared by Ar-ion milling and AsB images are taken. The contrast and the thickness of the reaction layer for an SOC of 5 % is too

low, hence only the samples with an SOC of 10 % are used for calculation. Due to the high contrast between the particle cross-section and the reaction layer in the AsB images of the samples with an SOC of 10 %, Figure 4b, the boundary of the particles can be easily determined. The resulting boundaries are shown in Figure 6b as black lines. Since the OsO_4 reaction layers are at least 100 nm thick and the SEI layer thickness is in the range of 20 - 60 nm, the threshold for the EASA detection is set to about 100 nm which corresponds to about three pixels in the AsB image (image pixel size: 38.66 nm/pixel). To obtain the EASA via image analysis, binary images of the carbon particles and pores as well as of the OsO_4 stained grain boundaries are obtained from the SEM image by thresholding. The overall grain-boundary is determined from the binary image of the particles (black lines in Figure 6b) while the binary image of the OsO_4 stained grain boundary regions is used for the EASA applying the three pixels mask as outlined before (red lines in Figure 6b). The ratio of black and red pixels is used to estimate the relative amount of the particle surface contributing to the EASA. The EASA values determined by this method are 37 %, 35 % and 72 % for the CG (155 µm x 59 µm), FG (227 µm x 27 µm) and AC (227 µm x 55 µm) samples, respectively.

The cross-sections can also be used for calculating the porosity (Φ). During the staining process, the Os reaction layer increases on the particle surface. The bright area in the AsB image (Figure 4 b) is therefore a fraction of the original porosity. Hence, the proportion of the porosity is one minus the areas of the grains divided by the total area of the cross-section (Eq. 3):

Eq. 3
$$\Phi = 1 - \frac{\sum grain\ areas}{Cross-section\ area}$$

The calculated porosity of the samples received by the cross-sections is 34 %, 54 % and 46 % for the CG, FG and AC samples, respectively. These results are in the same range as the calculated results in table 3 (see supplement).

There are some pores visible within the upper left particle in Figure 6 b). The surface of these pores did not react with the OsO$_4$, because these pores are a part of the internal porosity that did not have any contact with the Os vapor. Nevertheless, these pores are also considered in calculating the porosity.
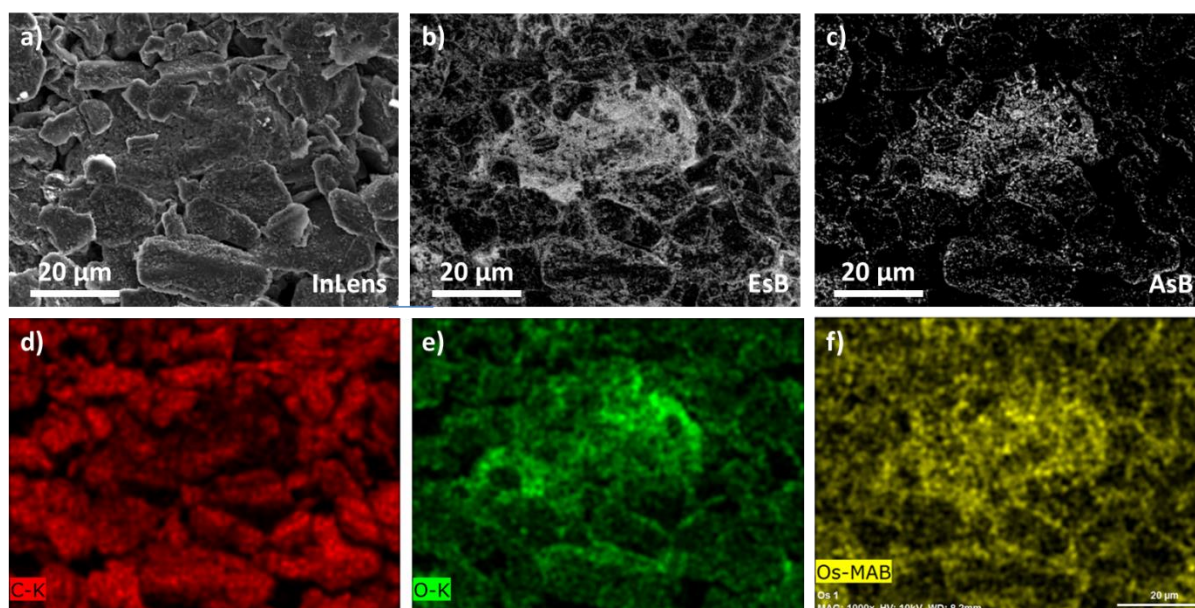

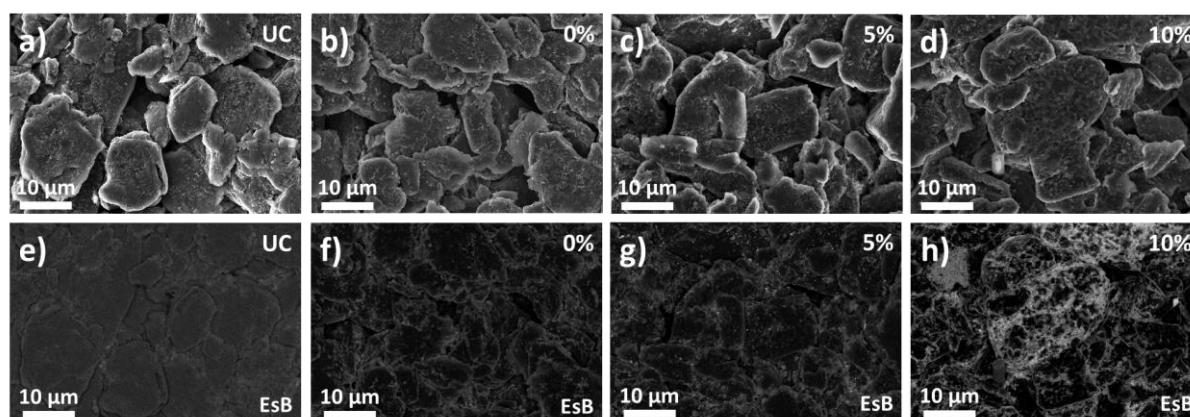Figure 2: InLens a), EsB b) and AsB c) images as well as EDX elemental maps of carbon d), oxygen e) and osmium f) taken at 10 keV of sample CG after 18 hours of staining.

Figure 3: SEM images of the CG sample with different SOC. The first row shows InLens, the second row EsB images. Each sample was exposed to the osmium tetroxide vapor for 18 hours. The SOC is shown in the upper right corner, whereas UC stands for uncycled.
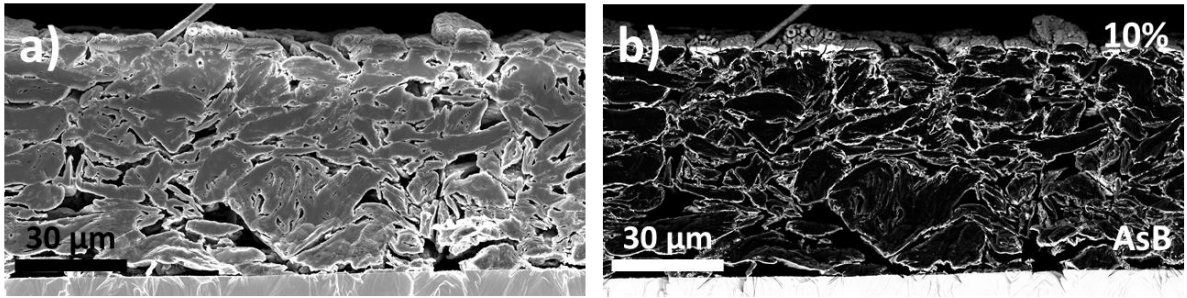
Figure 4: Cross-section of the CG sample after 18 hours of staining. The SEM InLens image a) and the AsB image b) show a 155 µm wide part of the cross-section. The copper-foil substrate is located at the bottom of the SEM images.
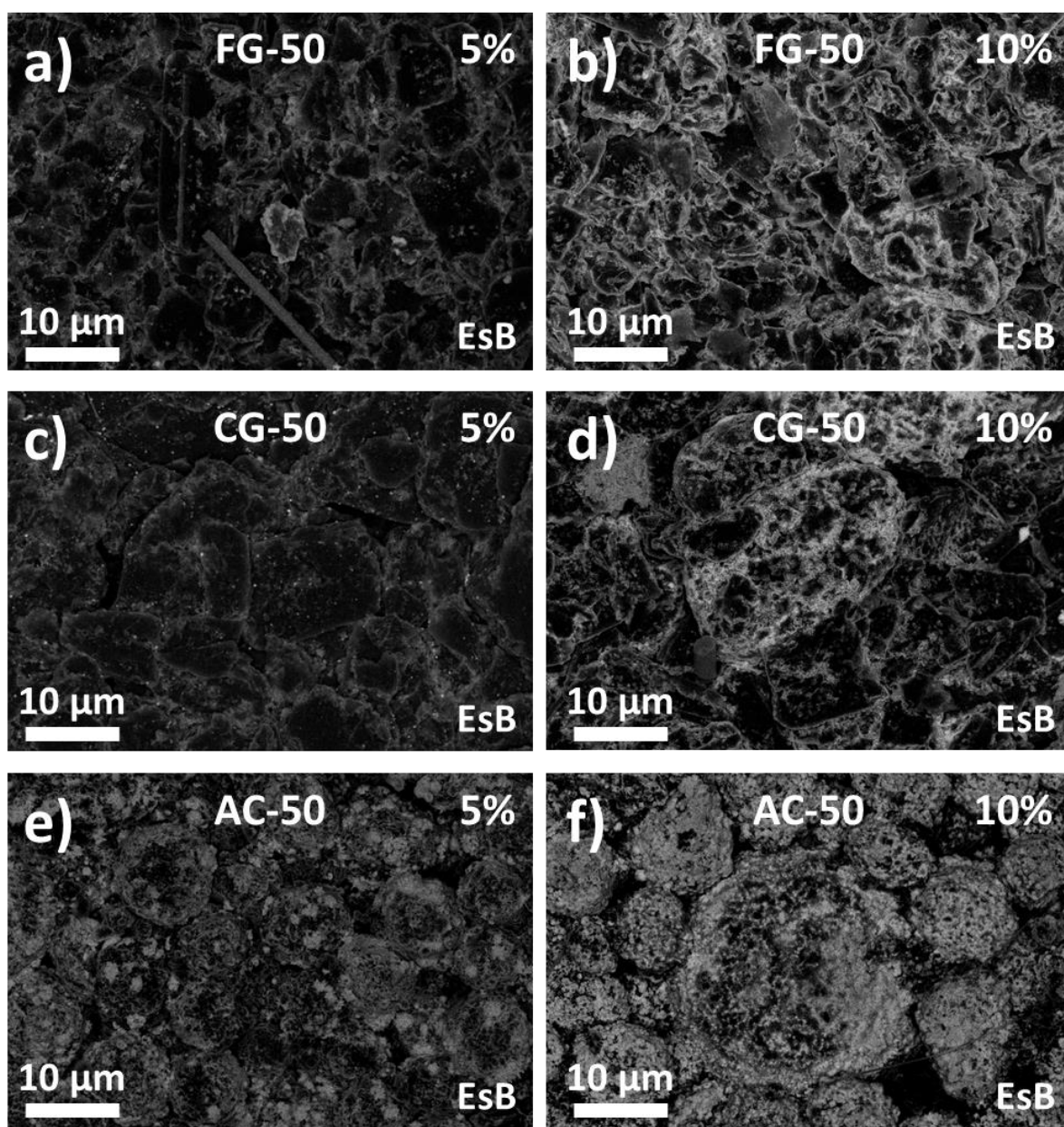
Figure 5: SEM-EsB images of the samples FG, CG and AC with an SOC of 5 % (left) and 10 % (right). The brightness in the image a) is increased by 30 % due to the low contrast of the electrode.
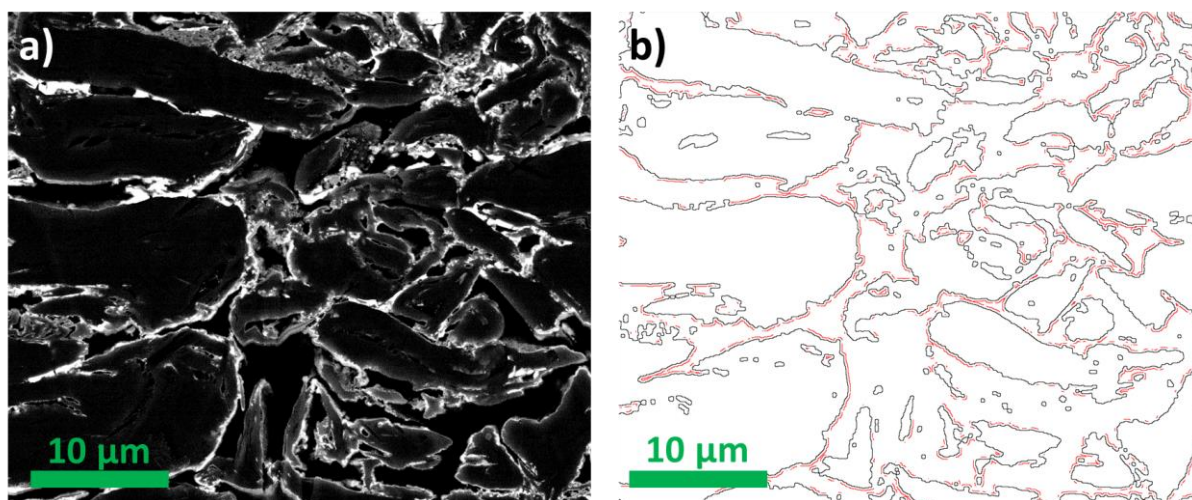
Figure 6: AsB image a) shows a part of the 155 µm wide cross-section of the CG sample with an SOC of 10 %. The grain boundary (black line) and the EASA (red line) are shown in b). The overall calculation yields an EASA of 37 %.

4 Determination of diffusion coefficients based on PITT measurements

The overall surface of anode active materials can be measured using the BET technique (see section 2.1). The areas determined in this manner do not represent the real EASA of the electrode. Thus, for measurements of the EASA that are incorporated in interfacial reactions, a special treatment using OsO_4 can be used, as mentioned previously.

Additionally, it is not clear that the entire active surface that is measured by the method using OsO_4 BET has the same contribution to the interface current in the Cottrell region, e.g. due to resistance gradients (see section 1). Thus, the electrochemical active surface area S_{EASA} can be limited by the upper limit S_u which is given by the BET surface of the structure and the lower limit S_l which is given by the base area of the electrode. This is schematically shown in Figure 7.
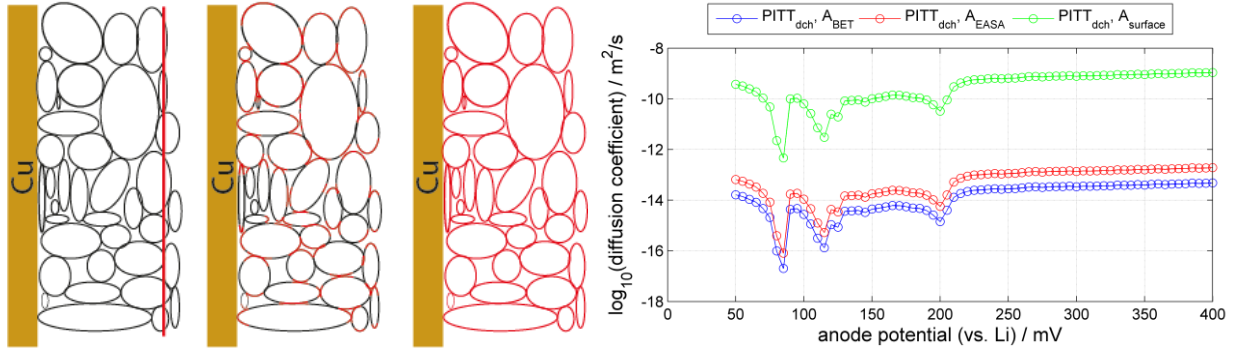
Figure 7: Left: Schematic approximation of described EASA-boundaries (left: lower limit S_l, middle: electrochemical active structure S_{EASA}, right: upper limit S_u), where black color represents non-EASA and red color EASA; right: Exemplary calculated diffusion coefficients for all cases described at left)

Based on these values the upper and lower boundaries for the diffusion coefficients D_l and D_u are calculated. Furthermore, we calculated the diffusion rate for the electrochemically active surface area D_{EASA} determined by OsO_4 staining (Table 2), which is in the range of the common results from the literature (see Table 2).

Table 2: Diffusion coefficients determined from literature for different carbon materials

literature	Type of carbon	Diffusion coefficient / $m^2 \cdot s^{-1}$
[3]	Artificial graphite (50% SOC)	1.24×10^{-13}
[3]	MCMB (50% / 100% SOC)	2.10×10^{-13} / 5.24×10^{-14}
[17]	Natural graphite	$10^{-12} \ldots 10^{-15}$ (dependent on type of measurement and SOC)
[17]	MCMB	$10^{-11.7} \ldots 10^{-15.7}$
[17]	Graphite	$10^{-11} \ldots 10^{-15}$
[17]	HOPG (bulk)	$3.84 \times 10^{-15} \ldots 1.42 \times 10^{-16}$

This is carried out for all tested samples (AC, CG and FG) described above and by example as shown in Figure 7b). It is important to note that the scale is logarithmic, because the upper

and lower limits differ by fife magnitudes. One can see that the lower boundary is not useful as calculated coefficients differ considerably from those referenced in the literature. For improvement of graphical presentation, only diffusion coefficients for the BET surface and EASA, respectively, were calculated (cf. Figure 8).
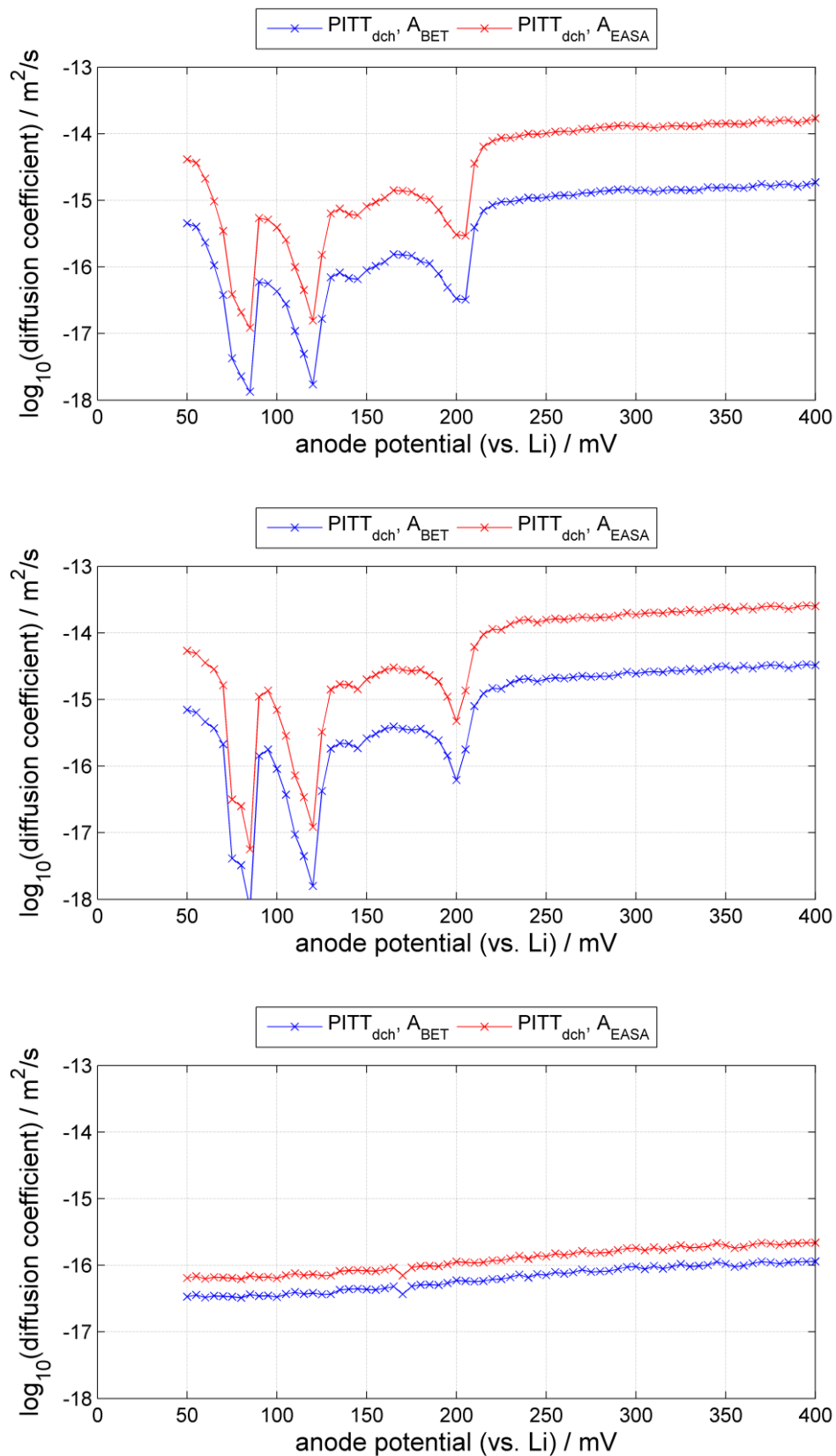
Figure 8: Diffusion coefficient calculated in the Cottrell region of PITT tests for different anode potentials of the sample used (red: determined EASA, blue: upper boundary from PITT test for intercalation process), top: FG, middle: CG, bottom: AC

The calculated diffusion coefficients, in particular those assuming the EASA fraction determined, are consistent with the literature e.g. as summarized in Table 2. In **Fehler! Verweisquelle konnte nicht gefunden werden.**, it can be observed that fine and coarse graphite show similar behavior, whereas amorphous graphite differs considerably. The most significant differences are that no phase transitions could be observed during PITT measurement of the samples. In agreement with [18] three transitions – in detail stage I to stage II (at ~80 mV), stage II to phase V (at ~130 mV) and phase V to sparse graphite (at ~210 mV) – could be seen. During the transitions, a poorer coefficient has been calculated, which can be explained by reorganization of the lithium placement within the graphite particles. Finally, we would like to conclude that apparent diffusion characteristics of amorphous carbon are worse than those from graphitic structures (neglecting the drops within phase transitions) as diffusion coefficients differ by a factor of 10 to 100.

5   Conclusion

Three different carbon-based materials (coarse graphite CG, fine graphite FG and amorphous carbon AC) are utilized to build lithium half cells. Anodes with an SOCs of 0 %, 5 % and 10 % are stained with osmium tetroxide. Due to the reaction of OsO_4 with lithiated carbon preferentially at graphitic edge sites the electrochemically active surface areas (EASA) could be visualized by electron microscopy. From SEM images, a calculation of the overall EASA of the different carbon electrodes is possible. The EASA of the graphitic carbon materials is about one third of the electrode surface, whereas the EASA of the amorphous carbon is approximately three quarters. In a further step, the upper and lower diffusion coefficients D_l and D_u are deduced for all materials based on previously conducted PITT measurements. It could be demonstrated that the diffusion behavior of the fine and coarse graphite is quite similar. Both showed potential dependent phase transition steps at approximately 80, 130 and 210 mV. During these intercalation steps, the diffusion coefficient dropped sharply due to reorganization of the lithium placement within the particles. Contrary to this, amorphous graphite displayed no phase transition steps. Moreover, its poorer diffusion characteristics as compared to fine and coarse graphite could be seen in a 10 to 100 times lower diffusion coefficient.

6   References

[1]   N. Legrand, B. Knosp, P. Desprez, F. Lapicque, S. Raël, Physical characterization of the charging process of a Li-ion battery and prediction of Li plating by electrochemical modelling, J. Power Sources. 245 (2014) 208–216. doi:10.1016/j.jpowsour.2013.06.130.

[2]   M. Wohlfahrt-Mehrens, C. Vogler, J. Garche, Aging mechanisms of lithium cathode materials, J. Power Sources. 127 (2004) 58–64. doi:10.1016/j.jpowsour.2003.09.034.

[3]   G. Hua-jun, L. Xin-hai, Z. Xin-ming, W. Hong-qiang, W. Zhi-xing, P. Wen-jie, Diffusion coefficient of lithium in artificial graphite , mesocarbon microbeads , and disordered carbon, 22 (2007). doi:10.1016/S1872-5805(07)60006-7.

[4]   V.A. Sethuraman, L.J. Hardwick, V. Srinivasan, R. Kostecki, Surface structural disordering in graphite upon lithium intercalation/deintercalation, J. Power Sources. 195 (2010) 3655–3660. doi:10.1016/j.jpowsour.2009.12.034.

[5]   F. Béguin, F. Chevallier, C. Vix-Guterl, S. Saadallah, V. Bertagna, J.N. Rouzaud, et al., Correlation of the irreversible lithium capacity with the active surface area of modified carbons, Carbon N. Y. 43 (2005) 2160–2167. doi:10.1016/j.carbon.2005.03.041.

[6]   F. Sagane, R. Shimokawa, H. Sano, H. Sakaebe, Y. Iriyama, In-situ scanning electron microscopy observations of Li plating and stripping reactions at the lithium phosphorus oxynitride glass electrolyte/Cu interface, J. Power Sources. 225 (2013) 245–250. doi:10.1016/j.jpowsour.2012.10.026.

[7]   A. Mukhopadhyay, B.W. Sheldon, Deformation and stress in electrode materials for Li-ion batteries, Prog. Mater. Sci. 63 (2014) 58–116. doi:10.1016/j.pmatsci.2014.02.001.

[8]   K. Persson, V.A. Sethuraman, L.J. Hardwick, Y. Hinuma, Y.S. Meng, A. van der Ven, et al., Lithium Diffusion in Graphitic Carbon, J. Phys. Chem. Lett. 1 (2010) 1176–1180. doi:10.1021/jz100188d.

[9]   W. Weppner, R.A. Huggins, Determination of the Kinetic Parameters of Mixed-Conducting Electrodes and Application to the System LLSb, J. Electroanal. Chem. 124 (1977) 1569–1578.

[10]   E. Markevich, M.D. Levi, D. Aurbach, Comparison between potentiostatic and galvanostatic intermittent titration techniques for determination of chemical diffusion coefficients in ion-insertion electrodes, J. Electroanal. Chem. 580 (2005) 231–237. doi:10.1016/j.jelechem.2005.03.030.

[11]   M.D. Levi, D. Aurbach, Frumkin intercalation isotherm - a tool for the description of lithium insertion into host materials : a review, Electrochim. Acta. 45 (1999) 167–185. doi:10.1016/S0013-4686(99)00202-9.

[12]   M.D. Levi, E.A. Levi, D. Aurbach, The mechanism of lithium intercalation in graphite film electrodes in aprotic media. Part 2. Potentiostatic intermittent titration and in situ XRD studies of the solid-state ionic diffusion, 421 (1997) 89–97. doi:10.1016/S0022-0728(96)04833-4.

[13]   M.E. Spahr, H. Buqa, A. Würsig, D. Goers, L. Hardwick, P. Novák, et al., Surface reactivity of graphite materials and their surface passivation during the first electrochemical lithium insertion, J. Power Sources. 153 (2006) 300–311. doi:10.1016/j.jpowsour.2005.05.032.

[14]   M. Zier, F. Scheiba, S. Oswald, J. Thomas, D. Goers, T. Scherer, et al., Lithium dendrite and solid electrolyte interphase investigation using OsO4, J. Power Sources. 266 (2014) 198–207. doi:10.1016/j.jpowsour.2014.04.134.

[15]   M. Wiederspahn, Analytical Power for the Sub-Nanometer World: New Gemini II Column with Complete Detection System, Imaging Microsc. 11 (2009) 25–26. doi:10.1002/imic.200990055.

[16]   W. Kuo, M. Briceno, D. Ozkaya, Characterisation of Catalysts Using Secondary and Backscattered Electron In-lens Detectors, Platin. Met. Rev. 58 (2014) 106–110. doi:10.1595/147106714X680113.

[17] M. Park, X. Zhang, M. Chung, G.B. Less, A.M. Sastry, A review of conduction phenomena in Li-ion batteries, J. Power Sources. 195 (2010) 7904–7929. doi:10.1016/j.jpowsour.2010.06.060.

[18] a. Senyshyn, O. Dolotko, M.J. Muhlbauer, K. Nikolowski, H. Fuess, H. Ehrenberg, Lithium Intercalation into Graphitic Carbons Revisited: Experimental Evidence for Twisted Bilayer Behavior, J. Electrochem. Soc. 160 (2013) A3198–A3205. doi:10.1149/2.031305jes.

[19] N. Iwashita, C.R. Park, H. Fujimoto, M. Shiraishi, M. Inagaki, Specification for a standard procedure of X-ray diffraction measurements on carbon materials, Carbon N. Y. 42 (2004) 701–714. doi:10.1016/j.carbon.2004.02.008.

[20] R.E. Franklin, The structure of graphitic carbons, Acta Crystallogr. 4 (1951) 253–261. doi:10.1107/S0365110X51000842.

[21] S. Flandrois, B. Simon, Carbon materials for lithium-ion rechargeable batteries, 37 (1999) 165–180. doi:10.1016/S0008-6223(98)00290-5.

7 Supplement

7.1 Characterization of carbon active materials

Particle size was measured by means of static laser light scattering (LA 950 particle analyzer, Horiba) in 2-propanol as dispersion liquid (after external ultrasonic treatment for de-agglomeration).

The specific surface area of the carbon materials was evaluated by the BET method (Gemini VII 2390 Surface Area Analyzer, Micromeritics). Prior to measuring, the specimens were dried for 12 hours at 120 °C in a vacuum.

The lattice parameters and degree of graphitization were determined by XRD (Siemens D5005, Cu-Kα radiation) according to [19]. To avoid peak broadening, only a thin layer of approximately 200 μm of carbon material (including Si as internal standard) was prepared. The interlayer spacing d_{002} was derived from the 002 Bragg-diffraction. On the basis of interlayer spacing d_{002} (nm), the degree of graphitization g was calculated following eq. 4 (Table 2). Within the limits of 0.3440 nm (lowest value for turbostratic carbon) to 0.3354 nm (ultimate value for graphite), the degree of graphitization g increases with decreasing interlayer spacing [20,21].

Eq. 4
$$g = \frac{0.3440 - d_{002}}{0.3440 - 0.3354}$$

Table 3: Crystallinity of carbon raw materials

Sample	Crystallinity	
	d_{002} / nm	g / %
CG	0.3359	94
FG	0.3360	93
AC	n/a	

7.2 Electrode preparation

For the preparation of the slurries, the active materials were dispersed together with carbon black (C-NERGY™ SUPER C65, Imerys, BET = 59 m²/g) in a 2 wt.% solution of CMC (sodium carboxymethyl cellulose, CRT 2000 PA 07, degree of substitution 0.75-0.85, DOW Chemicals). Homogenization was carried out in a dissolver stirrer at 2,000 rpm for 20 minutes. Finally, the SBR (styrene-butadiene-rubber) latex binder (TRD 2001, JSR Micro) was added at 500 rpm for 2 minutes, and entrapped air was removed by gently stirring in a vacuum. The relative mass composition of the slurry's solid content was as follows: active material/carbon black/SBR/CMC = 100/2/3/1.85. Immediately after preparation, the slurries were cast onto copper foil (Nippon Foil, 10 μm) using a continuous coater (KTF-S, Mathis AG) equipped with doctor blade technology and a double-field dryer. The coating speed was 0.2 m/minute and the foils were in-line dried within 10 minutes at 70 °C and 90 °C, respectively. In a subsequent calendaring step (GKL 200, Saueressig GmbH), porosity and surface roughness were reduced at a roll temperature of 60 °C. The final layer thickness was varied in order to validate its influence on the electrochemical performance and potentially on the diffusion of electrolyte and lithium ions during cycling to values of approximately 50 μm and 120 μm, respectively. Finally, the coated Cu-foils were vacuum-dried at 160 °C for 1 hour to improve the adhesion strength of the SBR binder.

7.3 Electrode characterization

Table 2 compares geometrical characteristics before and after calendaring of the carbon anodes; additionally, the areal mass loading − which is not affected by calendaring − is given in relation to the amount of the active material (93.5 wt.%). In spite of identical amounts of the inactive materials (binder, dispersant, conductive aid) and unmodified processing, the

dried anodes differ substantially in their inherent porosity, depending on the type of applied carbon. Before calendaring, the porosities of the flake-shaped coarse graphite electrodes reveal for both thickness grades a little bit over 50 %. In comparison, the finer graphite with similar morphology results in a higher porosity (60 %). Instead, the porosity of the AC 50 and 120 samples made of the spherical amorphous carbon particles is under 50 %.

In the course of the calendaring step, the porosity of anode layers was relatively reduced by 10 % for the AC and FG samples. The highest effect was observed for the CG 50 sample with a reduction of down to 36 %, which relates to a relative reduction of two-fifths, whereas the relative reduction value of the CG 120 sample is similar to the other.

Table 4: Properties of calendared and vacuum-dried electrodes

Sample	Before calendaring		After calendaring			
	Thickness (µm)	Porosity (%)	Thickness (µm)	Porosity (%)	Density (g/cm³)	Areal mass loading (mg/cm²)
CG 50	77	51.9	58	36.4	1.38	7.5
CG 120	140	50.7	120	42.2	1.26	14.1
FG 50	62	58.1	53	52.3	1.06	5.2
FG 120	137	60.0	117	53.9	0.99	10.9
AC 50	75	47.7	63	38.0	1.17	6.9
AC 120	129	48.2	119	42.8	1.06	11.9